Observing the loss and revival of long-range phase coherence through disorder quenches

Benjamin Nagler[a,b], Sian Barbosa[a,b], Jennifer Koch[a,b], Giuliano Orso[c,1], and Artur Widera[a,b,1]

[a]Department of Physics, Technische Universität Kaiserslautern, 67663 Kaiserslautern, Germany; [b]State Research Center for Optics and Material Sciences OPTIMAS, Technische Universität Kaiserslautern, 67663 Kaiserslautern, Germany; and [c]Laboratoire Matériaux et Phénomènes Quantiques, Université de Paris, CNRS, F-75013 Paris, France

Edited by Vanderlei Bagnato, Instituto de Física de São Carlos, Universidade de Sao Paulo, Sao Carlos, Brazil; received June 15, 2021; accepted November 18, 2021

Relaxation of quantum systems is a central problem in nonequilibrium physics. In contrast to classical systems, the underlying quantum dynamics results not only from atomic interactions but also from the long-range coherence of the many-body wave function. Experimentally, nonequilibrium states of quantum fluids are usually created using moving objects or laser potentials, directly perturbing and detecting the system's density. However, the fate of long-range phase coherence for hydrodynamic motion of disordered quantum systems is less explored, especially in three dimensions. Here, we unravel how the density and phase coherence of a Bose–Einstein condensate of $^6Li_2$ molecules respond upon quenching on or off an optical speckle potential. We find that, as the disorder is switched on, long-range phase coherence breaks down one order of magnitude faster than the density of the quantum gas responds. After removing it, the system needs two orders of magnitude longer times to reestablish quantum coherence, compared to the density response. We compare our results with numerical simulations of the Gross–Pitaevskii equation on large three-dimensional grids, finding an overall good agreement. Our results shed light on the importance of long-range coherence and possibly long-lived phase excitations for the relaxation of nonequilibrium quantum many-body systems.

ultracold quantum gases | disorder | nonequilibrium dynamics | interacting quantum systems

Macroscopic quantum phenomena such as superconductivity and superfluidity are central to our understanding of many-body quantum systems and play an important role in emerging quantum technologies (1). Their fascinating properties are tightly linked to the existence of a global wave function

$$\psi = \sqrt{n}e^{i\phi}, \quad [1]$$

with n being the density and ϕ being the quantum phase. Long-range phase coherence, that is, a fixed phase relation between far distant locations in the quantum system, is crucial for establishing superfluid properties in interacting systems (2). Microscopically, a large number of particles occupy the same quantum state phase coherently, as first recognized by Fritz London providing a description of the properties of superfluid ^{4}He (3), which has been successfully applied to the theoretical understanding and experimental control of Bose–Einstein condensates (BEC) in dilute atomic gases (4). The macroscopic quantum phase ϕ has been revealed in numerous interference experiments on BECs, including measurements of the first-order correlation function (5–8), its dynamics (9–11) in low-dimensional gases, and its statistics in disordered potentials (12). Moreover, it has been used as evidence for superfluidity in optical lattices (8) and in rotating traps generating vortices (13, 14).

The relaxation of such excited states is of central importance to our understanding of the nexus of superfluid and macroscopic realms, such as superfluid helium flowing along rough surfaces. For superfluid temperatures far below the transition point, it has been predicted that relaxation should occur free of dissipation as Kolmogorov-type turbulence (15). Experimentally, quantum dynamics of superfluids out of equilibrium were studied in various nonequilibrium realizations of superfluid helium (16–18), but also in turbulent relaxation of driven, ultracold quantum gases (19–21). However, different from interference of one-dimensional (1D) or 2D quantum fluids, the role of long-range phase coherence in nonequilibrium quantum dynamics and hydrodynamics is challenging to access experimentally for 3D systems. Quenches, that is, sudden changes of a system parameter, have proven to be a powerful tool for studying the nonequilibrium response of quantum systems. Examples include the collapse and revival of the matter wave field of a BEC (22), the transport of atoms in optical lattices (23, 24), and the response of quasi-particles upon a quench of interaction strength (25). Beyond spatially homogeneous or periodic quenches, lattice systems have also been quenched into disorder, and the response was interpreted to show signatures of a Bose glass phase (26). However, the behavior of long-range phase coherence following a quantum quench was not investigated in these works.

Here, we study the response of a BEC to quenches of an optical disorder potential. Recording the in situ density distribution and the expansion dynamics upon releasing the system from the trap, we can independently measure the responses of density and long-range phase coherence to the perturbation. Experimentally, we

Significance

Understanding the combined effects of disorder and interactions in quantum many-body systems is a key topic of condensed matter physics. While most studies have considered a static disorder, here we investigate the relaxation dynamics of a three-dimensional Bose–Einstein condensate after switching on or off an optical disorder potential. We study, experimentally and numerically, the transient and steady-state atomic density distribution and the ability of the gas to hydrodynamically expand, directly reflecting long-range phase coherence. We find that, when the gas is exposed to disorder, long-range phase coherence breaks down one order of magnitude faster than the density distribution responds. In the opposite case, surprisingly, long-range coherence takes two orders of magnitude longer times to revive than the density relaxation.

Author contributions: B.N. and A.W. designed research; B.N., S.B., and J.K. performed research; B.N. and G.O. analyzed data; B.N., S.B., J.K., G.O., and A.W. wrote the paper; and G.O. provided numerical simulations.

The authors declare no competing interests.

This article is a PNAS Direct Submission.

[1]To whom correspondence may be addressed. Email: Giuliano.Orso@univ-paris-diderot.fr or widera@physik.uni-kl.de.

This article contains supporting information online at https://www.pnas.org/lookup/suppl/doi:10.1073/pnas.2111078118/-/DCSupplemental.

Published December 30, 2021.

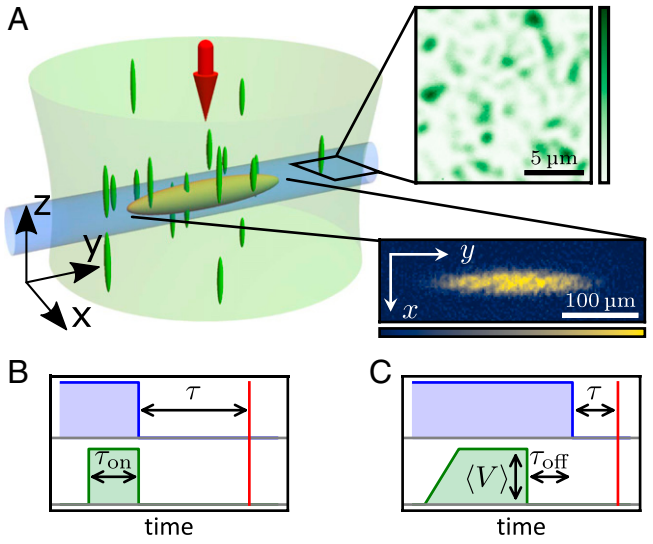

Fig. 1. Schematic illustration of the experimental setup and measurement sequences. (*A*) Experimental setup. The sample (yellow ellipsoid) is trapped in a superposition of an optical dipole trap (blue tube) and a magnetic saddle potential. The speckle beam (green volume) produces randomly distributed anisotropic grains. *Insets* show a section of the speckle intensity distribution in the *x*–*y* plane and an in situ absorption image of a BEC in disorder. (*B* and *C*) Sequences for quenches into and out of disorder, respectively. Blue: optical dipole trap depth; green: disorder strength; red: imaging pulse. For measurements probing the expansion dynamics, the optical dipole trap and disorder potential are instantaneously extinguished, and the gas is allowed to expand in the saddle potential for a variable time τ before the density distribution is recorded. The density dynamics are recorded in situ, that is, with $\tau = 0$.

prepare quasi-pure molecular BECs of typically 4×10^5 ^{6}Li$_2$ molecules in an elongated harmonic trap (Fig. 1) using standard techniques of laser and evaporative cooling (*Materials and Methods*). The trapping potential is a superposition of an optical dipole trap and a magnetic saddle potential, the latter being anticonfining in the z direction. The trapping frequencies are $(\omega_x, \omega_y, \omega_z) = 2\pi \times (164, 22.6, 107)$ Hz, leading to typical peak densities of $n_0 = 3.7 \times 10^{12}\,\mathrm{cm}^{-3}$ at the cloud center. We tune the interaction utilizing a magnetic Feshbach resonance, enabling us to adjust the *s*-wave scattering length a between the molecules (27). We use the gas parameter $n_0 a^3$, which relates a to the intermolecular distance $\propto n_0^{-1/3}$, to quantify the interaction strength. Subsequently, a repulsive optical speckle disorder potential $V(\mathbf{r})$ composed of 532-nm laser light and with a typical grain size $\eta_{x,y}^2 \times \eta_z = (750\,\mathrm{nm})^2 \times 10\,\mu\mathrm{m}$ is superimposed on the cloud, where $\eta_{x,y}$ and η_z are the correlation lengths along the respective directions (*SI Appendix* and 28). We characterize the disorder strength by its spatial average $\langle V \rangle$, which also coincides with the SD $\sqrt{\langle V^2 \rangle - \langle V \rangle^2}$ of the distribution.

The dynamics of a condensate in a speckle potential was first addressed experimentally (29) and theoretically (30) for elongated samples. The introduction of the random potential affects the BEC in two ways. First, the density distribution n readjusts to the altered external potential in order to minimize the energy of the system. Second, the phase is locally and dynamically shifted by $\Delta\phi(\mathbf{r}) = V(\mathbf{r})t/\hbar$ (31), where $\hbar$ is the reduced Planck constant and t is the illumination duration. Importantly, for quantum fluids, both effects are coupled via the velocity field (31)

$$\mathbf{v} = \frac{\hbar}{m}\nabla\phi, \qquad [2]$$

because a phase gradient is the source of a flow of density current $n\mathbf{v}$. The condensate can react to a spatial perturbation on a length scale given by the healing length $\xi = 1/\sqrt{8\pi n_0 a}$. In our experiment, the healing length at the trap center is below but of the order of the disorder grain size for all interaction strengths considered (*SI Appendix*). Therefore, the condensate wave function resolves the spatial fluctuations of the speckle amplitude (32).

Density versus Phase Response

To unravel how density and long-range phase coherence relax under a disorder quench, we perform two different kinds of experiments. First, we measure the in situ density distribution $n(x, y)$, column-integrated along the z direction via resonant absorption imaging. Molecules are repelled from the regions of large potential, leading to spatial density variations, albeit no total fragmentation, the classical percolation threshold being far below the chemical potential (33). We then quantify the degree of density variations of these images as

$$\sigma = \sqrt{\langle \Delta n^2 \rangle - \langle \Delta n \rangle^2}, \qquad [3]$$

where $\Delta n = n - n_{\mathrm{fit}}$ is the difference between n and a fitted 2D Thomas–Fermi profile n_{fit}, and the brackets denote averaging over all pixels of the absorption image where $n_{\mathrm{fit}} > 0$ (see *Materials and Methods*). In general, σ is nonzero even in the absence of disorder, since the finite imaging resolution, as well as thermal effects, cause deviations of the density distribution from the expected Thomas–Fermi profile. In the following, we subtract this contribution and focus on the disorder-induced density response. The disorder effect on the density at long times is shown in Fig. 2*A*, where the speckle is either introduced adiabatically, within 50 ms, or through a quench. In the first case, the degree of density variations σ increases monotonously with the disorder strength, while, in the second case, it grows faster for weak disorder but then saturates once the mean speckle potential $\langle V \rangle$ approaches half the chemical potential μ. Below, we use the time evolution of σ to quantify the response of the cloud's density to the disorder quench.

Second, we investigate the long-range phase coherence response by studying the expansion of the quantum gas upon release from a confining potential. The ensuing dynamics is entirely different from, for example, a noninteracting, thermal cloud. The existence of a wave function ψ implies collective dynamics similar to the hydrodynamic behavior of frictionless fluids (31, 34). Such coherent hydrodynamics leads to an inversion of the cloud aspect ratio during expansion from an anisotropic trap, which is a strong indication for BEC (4). Coherent hydrodynamics originates from the existence of a macroscopic wave function, hence long-range coherence, and facilitates collective behavior such as quadrupole excitations. By contrast, the collisional hydrodynamic behavior in nondegenerate systems with strong interactions (35, 36), such as unitary gases, is caused by frequent scattering events during expansion and is therefore not connected to a macroscopic wave function.

Expansion is initiated by extinguishing the dipole trap beam and letting the cloud evolve in the stationary saddle potential. Coherent hydrodynamics manifests itself as a sharp peak in the aspect ratio during expansion (*Materials and Methods*), whose magnitude we use as a measure of long-range coherence, similar to a method proposed in ref. 37. Here, the aspect ratio is R_x/R_y, with R_x and R_y as the Thomas–Fermi radii in x and y directions obtained from fits to the 1D integrated column density distributions n. Fig. 2*B* shows the dynamics of the aspect ratio for two cloud temperatures T below and above T_c, the critical temperature for condensation. The aspect ratio of a quasi-pure BEC with $T \ll T_c$ features an initial exponential growth (due to the saddle point confinement) followed by a pronounced peak with a value around 10 at roughly a quarter trapping period along the long axis of the cloud. This behavior is attributed to the onset

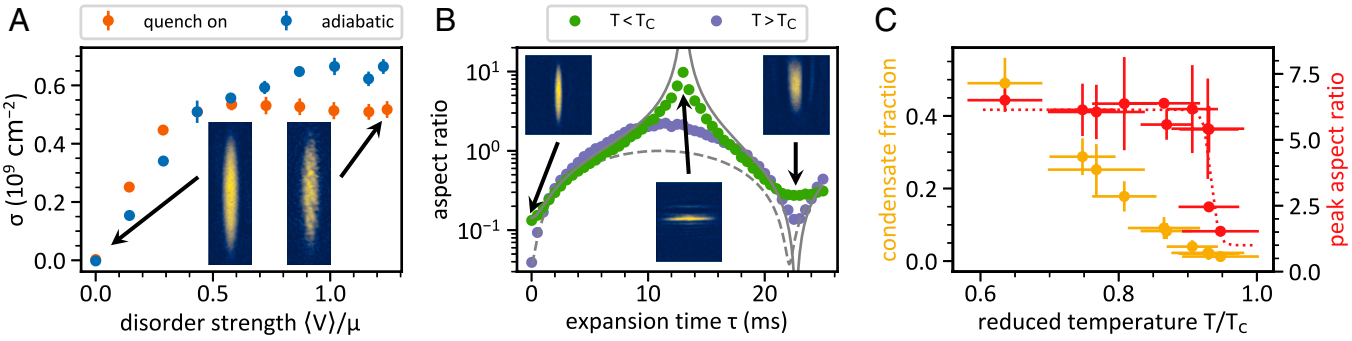

Fig. 2. Observables used to quantify the density and long-range phase coherence response upon disorder quenches. (*A*) Degree of density variation σ in the long time limit versus disorder strength, in units of the unperturbed chemical potential μ of the condensate, for $n_0a^3 = 1.1 \times 10^{-2}$; the speckle is introduced both adiabatically (blue) and through a quench (orange). *Insets* show absorption images for zero (*Left*) and maximum (*Right*) disorder strength, image sizes are 80 μm $\times$ 260 μm. The error bars are SDs of five repetitions and different disorder realizations. (*B*) Evolution of the cloud aspect ratio for $n_0a^3 = 1.1 \times 10^{-2}$ and temperatures above (purple) and below T_c (green) in the absence of disorder. The solid (dashed) line depicts the calculated trajectory for coherent hydrodynamic (ballistic) expansion (*Materials and Methods*). For short times, the measured trajectory for $T < T_c$ agrees well with the calculated one. For longer times, imaging aberrations due to the accelerating motion of the cloud along the imaging axis distort the measured aspect ratios, but qualitative agreement remains. *Insets* show absorption images for the case $T < T_c$ after 0, 13, and 23 ms of expansion, image sizes are 270 μm $\times$ 270 μm. (*C*) Condensate fraction and peak aspect ratio versus reduced temperature for $n_0a^3 = 0.4 \times 10^{-3}$ in the absence of disorder. Here, T_c is the critical temperature of a noninteracting gas in a harmonic trap (31). The dotted line serves as a guide to the eye.

of quadrupole oscillations, indicating long-range coherence. This is emphasized by Fig. 2*C*, which directly connects the onset of coherent hydrodynamics, quantified by the peak aspect ratio during expansion, with the appearance of a condensate fraction in the cloud, and, therefore, of a macroscopic wave function. By contrast, the aspect ratio of a thermal cloud, for which $T > T_c$, varies slowly. The peak value of 2.5 is larger than 1, which is the expected value for a gas with negligible interactions. We attribute this to a short initial phase of collisional hydrodynamics (38) due to the relatively large *s*-wave scattering length of $a = 2706\,a_0$, where a_0 is the Bohr radius. We will use the peak aspect ratio to quantify the breakdown and revival of long-range phase coherence in the system after the disorder quench.

We parallel these two experimental investigations by large-scale numerical simulations of the Gross–Pitaevskii (GP) equation (39, 40) for a 3D interacting quantum gas at zero temperature (see *Materials and Methods* for details). The numerics takes into full account the specific properties of the speckle pattern used in the experiment. We emphasize that the study of the hydrodynamic expansion of the condensate is extremely challenging, because the initial wavefunction is affected by the disorder, implying that the analytical scaling ansatz (41) breaks down, and the numerical solution of the GP equation in the saddle potential requires huge grids. From the numerical simulations, we extract time-resolved quantities after a disorder quench, namely, the widths of the cloud and the column-integrated density, to directly compare with the experimental data. We obtain further insight into the many-body relaxation dynamics from the spatial and temporal dependence of the condensate phase. Although this quantity is not directly accessible in our experiment, the study of its autocorrelation function (see Eq. **12** in *Materials and Methods*) provides a natural explanation of the characteristic time scales for the loss and revival of long-range phase coherence observed in the experiment.

Response to Quenches into Disorder

First, we focus on the system's response upon quenches into disorder, tracing the decay of the unperturbed BEC properties. We instantaneously ($< 1\,\mu$s) apply the speckle to a BEC for a time $\tau^{\rm on}$ (Fig. 1*B*). The density response is evaluated by imaging the cloud in situ after $\tau^{\rm on}$ and recording the emerging density variations $\sigma(\tau^{\rm on})$. For the coherence response, the dipole trap is extinguished after $\tau^{\rm on}$, and we record the peak aspect ratio during expansion as a function of $\tau^{\rm on}$.

Typical density and coherence response dynamics upon quenches into disorder are shown in Fig. 3. Globally, the cloud size (Fig. 3*A*) exhibits an initial steady growth along the strongly confined x axis, while the weakly confined y axis is almost unaffected. This effect, which is well reproduced by our numerics, originates from the fact that atoms are pushed off by the repulsive speckle potential, and, due to the small Thomas–Fermi radius $R_x = 18.5\,\mu$m, they cannot rearrange along this axis without increasing the system size.

By contrast, both phase and density variations respond much faster to the disorder quench (Fig. 3*B*). Long-range coherence rapidly disappears with increasing illumination duration $\tau^{\rm on}$, while the density variations develop approximately one order of magnitude slower than the coherence responds. We find this behavior to prevail for all parameters studied here. In the following, we denote the half-life period $\tau_{1/2}$ as the characteristic time after which density or coherence response have reached half their final value (*Materials and Methods*). In Fig. 3*C*, we summarize the half-life periods as a function of disorder strength. We find that the half-life periods decrease with disorder strength. Besides, we have investigated the influence of interaction strength on the dynamics and found slightly larger response times for decreasing interaction strength (*SI Appendix*).

An intuitive picture of the underlying mechanisms can be obtained from simple energy arguments (see *Materials and Methods* for details). For the density, after switching on the speckle, the random potential causes a spatially varying accumulation of phase and, therefore, a local velocity field according to Fig. 2. We are interested in the typical time $t_{\rm on}^{\rm d}$ after which the flow has traversed a given distance, which we set to the resolution of our imaging system $\alpha = 2.2\,\mu$m. Thus, we estimate the mean velocity from the average gradient $\propto \langle V\rangle/\eta_{x,y}$ of the local disorder potential, yielding $t_{\rm on}^{\rm d} \propto \sqrt{\alpha\eta_{x,y}/\langle V\rangle}$. This time scale is indicated in Fig. 3*C* as a solid blue line. Furthermore, we attribute the breakdown of coherent hydrodynamics to the phase imprint onto the BEC by the disorder potential, which is given by $\Delta\phi(\mathbf{r}) = V(\mathbf{r})\tau^{\rm on}/\hbar$. The phase pattern changes on length scales of the disorder correlation length, which is much smaller than the size of the quantum gas, and roughly a factor of 2 larger than the healing length of the condensate. Thus, the quench initiates a rapid and fine-grained phase evolution, eventually leading to dephasing between different locations within the cloud. From the mean phase difference $\langle\delta\phi\rangle = \langle V\rangle\tau^{\rm on}/\hbar$ between two points in the BEC, we deduce the time scale for breakdown of coherent hydrodynamics $t_{\rm on}^{\rm h} \propto \hbar/\langle V\rangle$. This time scale is indicated in

PHYSICS

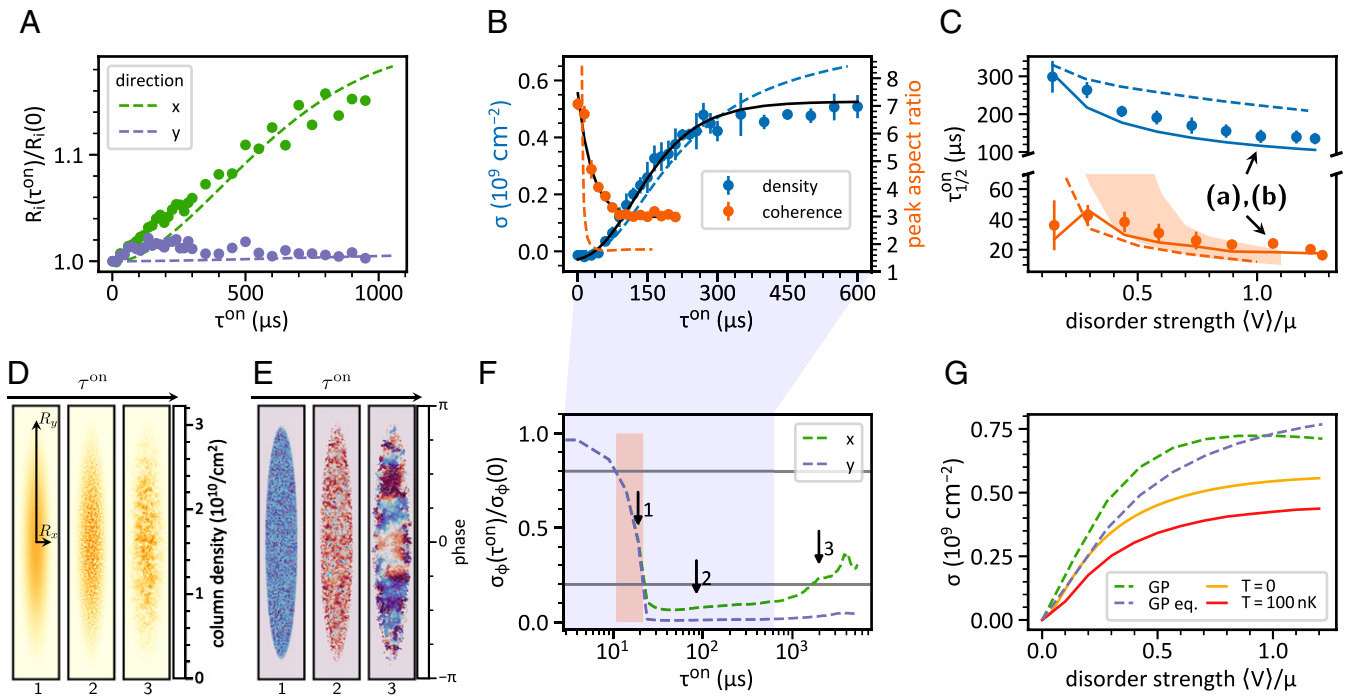

Fig. 3. Response of a quantum gas upon quenches into disorder. Symbols refer to experimental data, while dashed lines represent numerical results from the GP equation. (*A*) Time-resolved widths of the cloud, showing the broadening of the density distribution along the strongly confined axis. (*B*) Density response (blue) and peak aspect ratio during expansion (orange) as a function of the exposure time τ^{on}, based on a time series of quantum gas images for $\langle V\rangle/\mu = 1$ and $n_0 a^3 = 1.1 \times 10^{-2}$. Solid black line are fits to the data (*Materials and Methods*). The error bars are SDs of five repetitions and different disorder realizations. (*C*) Half-life periods of emerging density variations (blue) and the breakdown of coherent expansion (orange) for variable disorder strength and $n_0 a^3 = 1.1 \times 10^{-2}$, extracted from decay curves as *B*; the arrows point at the data points taken with the same experimental parameters as *A* and *B*. Error bars denote fitting uncertainties. The solid lines depict $t^{\mathrm{d}}_{\mathrm{on}}$ (blue) and $t^{\mathrm{h}}_{\mathrm{on}}$ (orange) as defined in the text. The $t^{\mathrm{h}}_{\mathrm{on}}$ incorporates the difference between the initial and final aspect ratio, which approaches zero for vanishing disorder strength (*Materials and Methods*). The orange shaded area displays the decay times of the phase correlation length shown in *F*, where the gray lines indicate two different threshold values used to extract the decay time. From the simulated wave function dynamics, we extract (*D*) the integrated column density and (*E*) the phase in the central plane at different times. (*F*) Normalized phase correlation length, extracted from column density and phase distributions. The arrows indicate the times τ^{on} for which the column density and phase distributions are shown in *D* and *E*. (*G*) The computed density responses at equilibrium and in the steady state (dashed lines) compared with the predictions based on the LDA for a gas at equilibrium at $T = 0$ and $T = 100$ nK (solid lines).

Fig. 3*C* as a solid orange line and reproduces well the trend of the experimental data.

Next, we compare our GP numerics with the experimental data. We obtain time-resolved column density and in-plane phase distributions, as shown in Fig. 3 *D* and *E*, respectively. The density response is then computed by first convolving the density data with a Gaussian function of width 2.2 μm, to account for the limited resolution of the imaging system (*SI Appendix*). The result agrees reasonably well with the measured data, although numerics predicts a larger value of σ in the steady state, which, in turn, leads to a larger half-life period, as shown in Fig. 3 *B* and *C*. In Fig. 3*G*, we plot the density response as a function of the disorder strength, calculated both at equilibrium and in the steady state, following the disorder quench. The obtained results are in good agreement with the experimental data shown in Fig. 2*A*. A closer comparison reveals that the numerics overestimates σ, especially when the disorder is strong. We attribute this residual difference to finite temperature effects, which are neglected in the GP equation. To understand the role of temperature, we compute the density response of the disordered gas at equilibrium via the local density approximation (LDA), both at $T = 0$ and at $T = 100$ nK, by using the Hartree–Fock approach (see *Materials and Methods*). The results are plotted in Fig. 3*G* with solid lines. Two comments are in order here. First, while, for weak disorder, the LDA result for the disorder-induced density response at zero temperature is indistinguishable from the prediction of the GP equation, for strong disorder, the LDA result falls below it. Indeed, LDA underestimates the atom density in the center of the trap, which contributes mostly to the signal, while it overestimates the density at the periphery. Second, even if the gas is in the quantum degenerate regime, thermal effects can broaden the density distribution and deplete the density response.

Let us now discuss the GP results for the hydrodynamic expansion of the BEC, after exposure to the speckle potential. The calculated peak aspect ratio and the associated half-life period, displayed in Fig. 3 *B* and *C*, respectively, reproduce the experimental trend, although with much faster decay of long-range phase coherence for short illumination times, because the GP numerics does not account for imaging aberration effects. Notice that the difference in the peak aspect ratio observed for large τ^{on} is mainly due to the large in-plane grid spacings used for the expansion dynamics (*SI Appendix*). Notwithstanding, the separation of time scales for density and phase relaxations is recovered, and even accentuated, by the GP numerics.

The disorder-induced loss of long-range coherence can be directly related to the scrambling of the condensate phase before the expansion. From the snapshots of density and phase distributions as in Fig. 3 *D* and *E*, we extract the time-resolved phase correlation function (*Materials and Methods*) of the BEC. The result is shown in Fig. 3*F*. We see that the phase correlation length σ_ϕ drops around $\tau^{\mathrm{on}} = 20$ μs, which roughly corresponds to the observed half-life period in Fig. 3*C*. We repeat the analysis for different disorder strengths. We consider a range of phase

correlation lengths between 0.2 and 0.8 of the maximum value and extract the time scale on which these correlation lengths are reached, indicated by an orange shaded area in Fig. 3*C*. The numerical values yield, indeed, the correct order of magnitude for the time response. We conclude that the density and phase responses of the quantum gas to disorder quenches can be unraveled by the two measurement methods. Overall, the loss of long-range phase coherence is typically one order of magnitude faster than the density relaxation.

Response to Quenches out of Disorder

Next, we consider the case when the quantum system relaxes after release from an initially disordered state and ask the question regarding when an unperturbed density distribution and long-range coherence are reestablished. Quenches out of disorder are realized by slowly introducing the speckle during a 50-ms linear ramp, in order to minimize excitations in the gas, and subsequently waiting for 100 ms to let it equilibrate. Then we suddenly extinguish the speckle and wait for a variable time $\tau^{\rm off}$, during which the system can relax (Fig. 1*C*), before probing the density variations or expansion dynamics.

For the density response, we do not find any dependence of the half-life period $\tau^{\rm off}_{1/2} \approx 250\,\mu$s on either disorder or interaction strength (Fig. 4 *B* and *F*). The final value of σ after the longest measured wait time of $\tau^{\rm off} = 1$ ms is up to 0.1×10^9 cm^{-2} above its value in the clean case for large disorder strengths (Fig. 4*A*).

By contrast, we find that it takes two orders of magnitude longer to restore long-range phase coherence, with a peak aspect ratio comparable in magnitude to the disorder-free case. This is consistently observed for all disorder strengths applied, as shown in Fig. 4*B*. Here, too, simple arguments allow relating the observed time scales to the energy scales of the system. The long time to reestablish coherent hydrodynamics can be compared to the longest time scale in the system, that is, the time $t^{\rm h}_{\rm off}$ a signal needs to traverse the long axis of the cloud with the speed of sound, $t^{\rm h}_{\rm off} = 2R_y/v_{\rm s}$, where R_y is the largest Thomas–Fermi radius of the BEC, and $v_{\rm s} = \sqrt{\mu/m}$ is the maximum speed of sound at the center of the cloud. Furthermore, we observe that both the density and the coherent response are rather independent of interactions in the gas (Fig. 4*F*). Importantly, there are no significant particle losses during $\tau_{\rm off}$ (*SI Appendix*). This excludes speckle-induced heating and subsequent evaporation as the origin of the breakdown and revival of coherent hydrodynamics. In the transient regime after the quench, the widths of the BEC along the x and y directions remain unchanged. The numerics shows that the BEC shrinks along the z direction, where the disorder potential varies slowly.

The GP simulations predict a rapid decay for the density response (Fig. 4*A*), which ultimately saturates to a nonzero value, as also found in the experiment. For sufficiently strong disorder ($\langle V\rangle/\mu \gtrsim 0.5$), the calculated density response features large-amplitude oscillations in the long time limit (after 1 ms), which are absent in the experimental data. The origin of this effect can be traced back to a corresponding oscillation of the Thomas–Fermi radii, especially along the strongly confined x axis. The compression of the cloud leads to an enhancement of the peak atom density, which, in turn, causes an increase in the density response. In the experiment, this collective mode is probably damped by the coupling between the BEC and the thermal component of the cloud (42). For this reason, the calculated

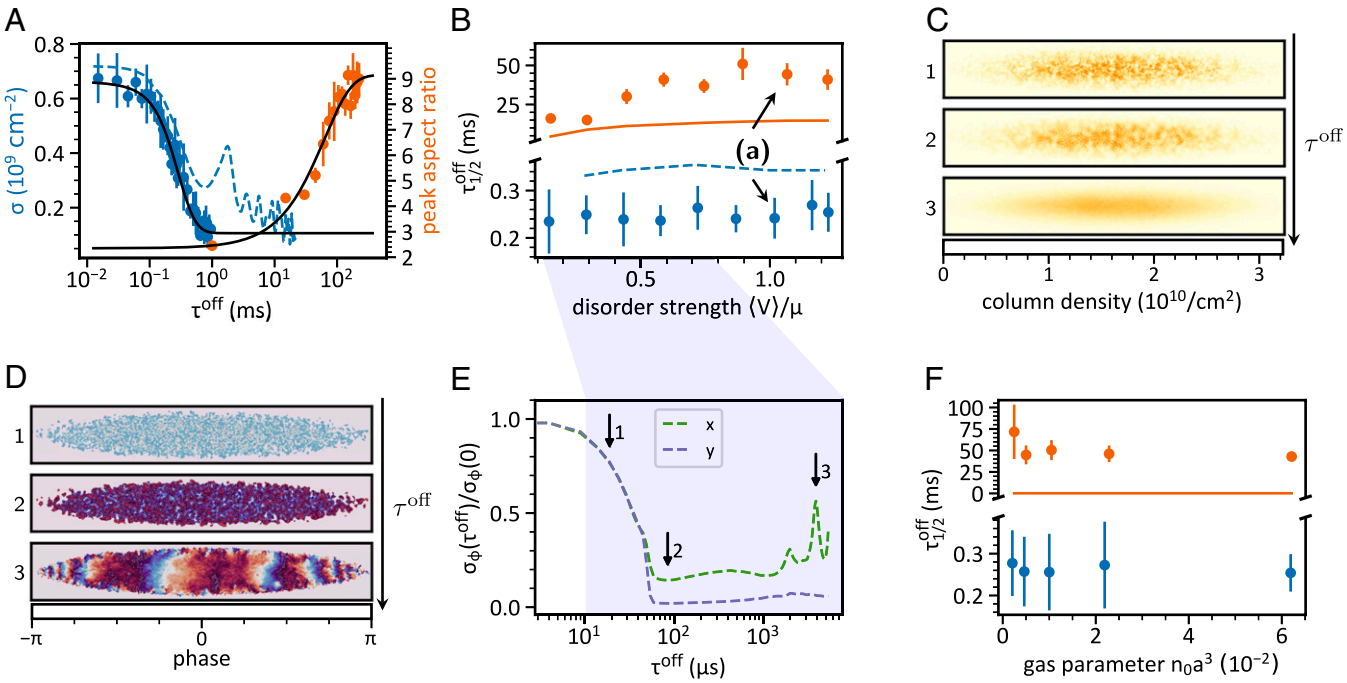

Fig. 4. Response of a quantum gas upon quenches out of disorder. Symbols refer to experimental data, while dashed lines represent numerical results from the GP equation. (*A*) Quantum gas dynamics showing decaying density variations (blue) and revival of coherent hydrodynamic expansion (orange) for $\langle V\rangle/\mu = 1$ and $n_0a^3 = 1.1 \times 10^{-2}$. The error bars are SDs of five repetitions and different disorder realizations. The black lines are fits to the experimental data (*Materials and Methods*). (*B*) Half-life periods of such dynamics as a function of disorder strength for a gas density of $n_0a^3 = 1.1 \times 10^{-2}$, where the error bars denote fitting uncertainties. For comparison, the solid line depicts $t^{\rm h}_{\rm off}$ as defined in the *Materials and Methods*, indicating the time scale to cross the long axis of the BEC with the speed of sound. Clearly, the time scale for revival of quantum hydrodynamics is much longer than the time scale $t^{\rm h}_{\rm off}$. Here, $t^{\rm h}_{\rm off}$ incorporates the difference between the initial and final aspect ratio. (*C* and *D*) Three different snapshots of the numerically simulated column density and in-plane phase distribution, respectively, following the quench. (*E*) Normalized phase correlation length σ_ϕ extracted from the two time-resolved distributions in *C* and *D*, showing the absence of long-range coherence within the simulated times. The arrows in *E* indicate the times $\tau^{\rm off}$ for which the column density and phase distributions are shown in *C* and *D*. (*F*) The half-life periods for variable interaction strength and $\langle V\rangle/k_{\rm B} = 145$ nK, where the solid line again indicates the time scale $t^{\rm h}_{\rm off}$ for comparison.

half-life period for the density response (Fig. 4*B*) is slightly larger than in the experiment. On the other hand, the calculation of the peak aspect ratio for values of τ^{off} of the order of tenths or hundreds of milliseconds is numerically heavy, due to growing errors, which affect the subsequent expansion dynamics. For this reason, we leave it for future studies. In Fig. 4 *C* and *D*, we display some snapshots of the column density and phase distributions following the disorder quench, from which we extract the phase correlation function (Fig. 4*E*). Within the simulated time intervals, we observe a progressive locking of the local condensate phase along the x axis. By contrast, the phase varies rapidly along the weakly confined y direction, signaling the presence of phonon-like excitations.

Conclusions

We have performed an experimental and numerical study of the far-from-equilibrium dynamics of a molecular BEC subject to a quench of the disorder potential. We have found that density and long-range phase coherence respond to the perturbation on different time scales. Specifically, the long times needed to restore long-range phase coherence might indicate the decay of a complex phase pattern toward an ordered phase, where, for instance, phase boundaries or vortices originating from the disorder quench are topologically robust and need a relatively long time to decay.

In the future, it will be interesting to study the dynamical response of quantum gases along the cross-over from a BEC to a Bardeen–Cooper–Schrieffer (BCS) type superfluid to explore the impact of quenched disorder on resonantly interacting superfluids. Our system is also ideally suited to follow further the phase dynamics and its dependence on quench parameters. Finally, our work calls for more refined numerical simulations of the dynamics of the disordered BEC, including finite temperature effects.

Materials and Methods

In the following, details on the experimental procedure and the theoretical models, as well as additional data, are given.

Setup and Sequence. A general overview of our experimental apparatus is presented in ref. 45. We prepare quantum gases in the BEC–BCS cross-over regime by forced evaporative cooling of fermionic ^{6}Li atoms in an equal mixture of the two lowest-lying Zeeman substates of the electronic ground state $^2S_{1/2}$. Evaporation takes place in a hybrid magnetic–optical trap at a magnetic field of 763.6 G on the repulsive side of a Feshbach resonance centered at 832.2 G (46), where atoms of opposite spin form bosonic molecules that eventually condense into a BEC. After evaporation, the sample is held at constant trap depth for 250 ms to ensure thermal equilibrium before the magnetic field is linearly ramped to its final value during 200 ms. We employ resonant high-intensity absorption imaging (47) to extract the column density distribution in the x–y plane. From bimodal fits to the in situ density distribution (48) at 680 G, we are not able to discern a thermal fraction.

This picture directly connects our observation to the recently reported absence of hydrodynamic behavior in BECs, where turbulence was introduced by applying a spatially homogeneous, oscillating force (21, 43). Numerical simulations show that random phase imprints, spatially varying on a length scale slightly larger than the healing length, also result in turbulent flow (44). Turbulence and accompanying vortices can be rather persistent, with lifetimes exceeding several hundred milliseconds (14, 21). This suggests that the phase dynamics ensuing after a disorder quench might generate turbulent flow that takes a relatively long time to decay before long-range phase coherence is established. The fact that we do not see a sign of this in the density distributions for times longer than ~ 1 ms after quenches might be explained by the limited optical resolution of $\alpha = 2.2$ μm of our imaging system and the integration of the density along the z axis. In turbulent flow, an energy cascade (21) could transfer excitations to smaller length scales we cannot resolve.

The hybrid trap consists of an optical dipole trap and a magnetic saddle potential, which provides weak (anti) confinement in (z) x and y directions, whereas the optical trap strongly constrains the cloud along x and z. Since the saddle potential is an accessory to the magnetic field used to address the Feshbach resonance, its curvature depends on the field magnitude. For all experiments presented here, the combined trapping frequencies of the optical and magnetic trap are $\omega_x = 2\pi \times 164$ Hz and $\omega_z = 2\pi \times 107$ Hz. ω_y is listed in *SI Appendix*, Table S1 for the different magnetic fields addressed.

The speckle potential is created by passing a laser beam of wavelength 532 nm through a diffusive plate and focusing the light, using an objective with numerical aperture 0.29, onto the atoms. They experience a repulsive and spatially random (but temporally constant) dipole potential V, which we characterize by its average $\langle V\rangle$ at the focal point of the objective. The typical grain size of the speckle is given by the Gaussian-shaped autocorrelation function of the potential with $1/e$ widths (correlation lengths) $\eta_{x,y} = 750$ nm transversely to and $\eta_z = 10$ μm along the beam propagation direction. As the speckle beam has a Gaussian envelope with waist 850 μm, the disorder potential is slightly inhomogeneous, with less than 5% variation of $\langle V\rangle$ across the typical cloud size. We change the specific disorder realization by slightly rotating the speckle pattern as a whole between repetitions. For that reason, the diffusive plate is attached to a motorized rotation mount. This allows us to measure disorder-averaged quantities that are independent of the microscopic details of any specific disorder realization. Switching on and off the speckle potential and letting the BEC equilibrate subsequently, we do not find a measurable increase of temperature.

Measurement of Density Variation. We quantify the degree of density variation of a measured column density distribution n as $\sigma = \sqrt{\langle \Delta n^2\rangle - \langle \Delta n\rangle^2}$ with $\Delta n = n - n_{\mathrm{fit}}$, see Fig. 5. Here n_{fit} is a smooth, two-dimensional Thomas–Fermi profile

$$n_{\mathrm{fit}} \propto \begin{cases} p^{3/2} & p > 0 \\ 0 & \text{else,} \end{cases} \qquad [4]$$

with $p = 1 - (x/R_x)^2 - (y/R_y)^2$, fitted to n. The brackets denote averaging over all pixels with $n_{\mathrm{fit}} > 0$. Due to imaging aberrations and inhomogeneities of the imaging setup, σ is larger than zero even for density profiles without disorder. We correct for that by subtracting this offset.

To extract the half-life period from the density response dynamics (Fig. 2*A*), we fit the time series with a Gompertz function $\propto \exp(-b\exp(-ct))$ (49). The half-life period is obtained by calculating $\tau_{1/2} = -\log(\log(2)/b)/c$, where log is the natural logarithm.

Cloud Expansion into a Saddle Potential. The time evolution of a BEC with initial density distribution $n(\mathbf{r}, t = 0)$ in a harmonic trap with time-dependent frequencies $\omega_i(t)$ ($i = x, y, z$) can be described in terms of a scaling transform $n(\mathbf{r}, t) = n(x/b_x, y/b_y, z/b_z, t)/b_x b_y b_z$ (41). The scaling parameters $b_i(t)$ are obtained from the solution of

$$\ddot{b}_i = -\omega_i^2(t) b_i + \frac{\omega_i(0)^2}{b_i b_x b_y b_z} \qquad [5]$$

with boundary conditions $b_i(0) = 1$ and $\dot{b}_i(0) = 0$. For our system, $(\omega_x(0), \omega_y(0), \omega_z(0)) = 2\pi \times (164, 22.6, 107)$ Hz for 763.6 G. With decreasing magnetic field, $\omega_y(0)$ also decreases slightly (*SI Appendix*, Table S1), while $\omega_x(0)$ and $\omega_z(0)$ are solely determined by the optical trap. Upon extinction of the dipole trap at $t = 0$, the trapping frequencies instantaneously take on the values $\omega_{x,y,z}(t) = \omega_y(0), \omega_y(0), i\sqrt{2}\omega_y(0)$.

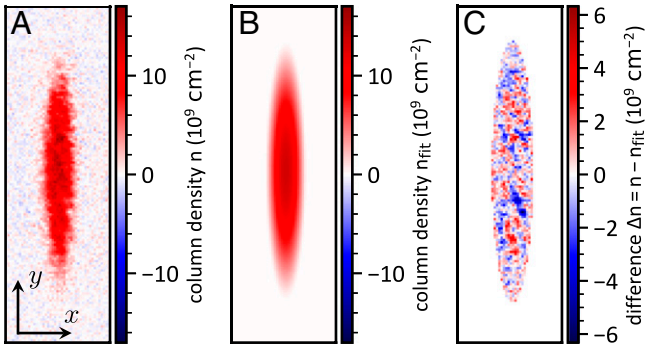

Fig. 5. Calculation of density variation σ from an exemplary density profile obtained at interaction strength $n_0 a^3 = 1.1 \times 10^{-2}$ and disorder strength $\langle V\rangle/\mu = 1.2$. (*A*) Measured density distribution n. (*B*) Fitted Thomas–Fermi profile n_{fit}. (*C*) Difference $\Delta n = n - n_{\mathrm{fit}}$ in the region where $n_{\mathrm{fit}} > 0$.

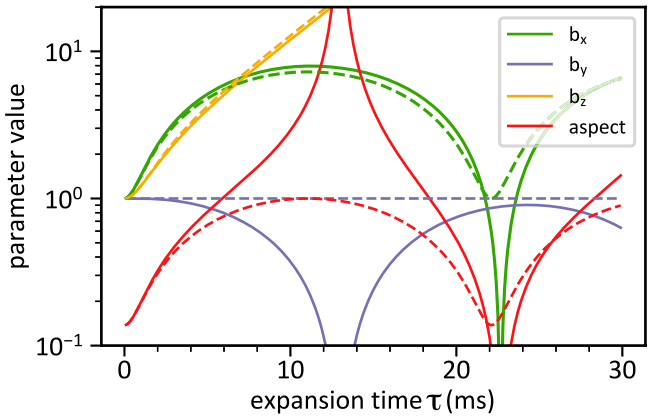

Fig. 6. Scaling parameters and aspect ratio for coherent hydrodynamic (solid lines) and ballistic (dashed lines) expansion into the saddle potential for a magnetic field of 763.6 G in our setup.

The imaginary frequency reflects the anticonfining nature of the saddle potential along z. Note that Eq. **5** neglects the contribution of the quantum pressure $\propto \nabla^2\sqrt{n}$ (31). Fig. 6 shows the dynamics of the scaling parameters during expansion. The reduction of the trapping frequency along the x axis causes an initial rapid expansion of the cloud in this direction and a concomitant contraction along the y axis, leading to the inversion of the aspect ratio. This effect is further amplified by the presence of the saddle potential along the z axis, stretching the cloud ever increasingly. In contrast, a noninteracting cloud does not exhibit collective behavior, and each particle escapes with its momentary velocity at the time of release. This facilitates an analytical description of such ballistic expansion dynamics in terms of a scaling transform (4); the corresponding trajectories are displayed in Fig. 6. The most distinct feature of hydrodynamic expansion, as compared to ballistic expansion, is the contraction and subsequent expansion of the cloud along its initially longer axis, causing an inversion of the aspect ratio.

Numerical Simulations of the Experiment.

Modeling the disorder. The disorder potential used in the experiment is a single, blue-detuned, anisotropic speckle with an on-site probability distribution given by the Rayleigh law, $P(V) = e^{-V/\langle V\rangle}\Theta(V)/\langle V\rangle$, where $\Theta(x)$ is the Heaviside function. The speckle pattern is generated by a laser beam parallel to the z axis and is characterized by the spatial correlation function (50)

$$C(\mathbf{r}) = \frac{\langle V(\mathbf{r})V(0)\rangle}{\langle V^2(0)\rangle} = \left|\frac{f(\mathbf{r})}{f(0)}\right|^2, \qquad [6]$$

where

$$f(\mathbf{r}) = \int_0^\pi e^{i2\pi\frac{z}{\lambda_L}\cos\theta} J_0\left(2\pi\frac{\rho}{\lambda_L}\sin\theta\right) h(\theta)\sin\theta \mathrm{d}\theta. \qquad [7]$$

Here, $\lambda_L = 532$ nm is the laser wavelength, $J_0(x)$ is the zero-order Bessel function, and $\rho = \sqrt{x^2+y^2}$. The function $h(\theta)$ in Eq. **7** depends on the specific experimental setup. Following ref. 51, we write it as

$$h(\theta) = \exp\left(-\frac{2\tan^2\theta}{\theta_0^2}\right)\Theta(\tan\theta_{\max} - |\tan\theta|), \qquad [8]$$

where $\theta_{\max}$ defines the maximal numerical aperture $NA = \sin(\theta_{\max}) = 0.29$ of the objective, while θ_0 is a free parameter. Its specific value is fixed to reproduce the measured correlation length $\eta_{x,y} = 750$ nm of the speckle in the x–y plane, which is defined as $C(x = \eta_{x,y}, 0, 0) = 1/e$. By substituting Eq. **8** into Eq. **7** and carrying out the numerical integration over the angle, we find that this condition is satisfied for $\theta_0 = 0.25$.

The speckle potential has been generated numerically on a 3D grid with uniform spacings $\Delta x = \Delta y = \Delta z = 0.3\lambda_L$. This is done by first generating, at each site j of the grid, a complex field E_j, whose real and imaginary parts are uncorrelated normally distributed random variables with zero mean and unity variance. The total electric field at position $\mathbf{r}$ is obtained by convolving the random field with an appropriate mask $\mathcal{P}(\mathbf{k})$ in Fourier space (33),

$$E(\mathbf{r}) = \sum_{\mathbf{k}} E(\mathbf{k})\mathcal{P}(\mathbf{k})e^{i\mathbf{k}\cdot\mathbf{r}}, \qquad [9]$$

so that the resulting speckle potential $V(\mathbf{r}) = \langle V\rangle|E(\mathbf{r})|^2/\langle|E|^2\rangle$ obeys the correlation function in Eqs. **6**–**8**. This yields $\mathcal{P}(\mathbf{k}) = \delta(|\mathbf{k}| - 2\pi/\lambda_L)\sqrt{h(\theta)}$, where the angle θ is defined by $k_z = |\mathbf{k}|\cos\theta$.

Numerical solution of the GP equation. At zero temperature, the BEC is described by a macroscopic wave function $\psi(\mathbf{r}, t)$ obeying the nonlinear mean-field GP equation (39, 40)

$$i\frac{\partial\psi}{\partial t} = \left[-\frac{\hbar^2}{2m}\nabla^2 + V_{\mathrm{tr}}(\mathbf{r}) + V(\mathbf{r}) + g|\psi(\mathbf{r}, t)|^2\right]\psi(\mathbf{r}, t), \qquad [10]$$

where $V_{\mathrm{tr}}(\mathbf{r}) = m(\omega_x^2x^2 + \omega_y^2y^2 + \omega_z^2z^2)/2$ is the harmonic confining potential, and $g = 4\pi\hbar^2a/m > 0$ is the strength of the boson–boson repulsion. The amplitude of the wave function is normalized according to $\int|\psi(\mathbf{r}, t)|^2\mathrm{d}^3r = 1$ and is related to the 3D particle density through $n_{3D}(\mathbf{r}, t) = N|\psi(\mathbf{r}, t)|^2$. The ground-state density profile of the BEC is obtained from the GP equation via imaginary time propagation. In the absence of disorder, the Thomas–Fermi radii of the condensate are $R_x = 18.5$ μm, $R_y = 134.4$ μm, and $R_z = 28.4$ μm. The numerical integration of the GP equation for the trapped gas is carried out on a grid of fixed dimensions $(N_x, N_y, N_z) = (300, 2{,}200, 450)$ and uniform spacing $\Delta x = \Delta y = \Delta z = 0.16$ μm. We use the open-source code presented in refs. 52 and 53, implementing the split-step Crank–Nicholson method. Simulating 1 ms of time evolution for a given disorder configuration requires between 1 and 2 h of wall clock time on an Intel Haswell node with 24 CPU cores.

The maximum value of the aspect ratio during the expansion is reached after (roughly) $t = 13$ ms. GP simulations for such long time scales are difficult, also because the BEC widths along the x and z axes grow rapidly with time, requiring exceedingly large grids. In particular, the anticonfining potential accelerates the particles outward, implying that a fine mesh is necessary to follow the rapid spatial oscillations of the wave function and avoid numerical instability at the condensate tails. We simulate the expansion dynamics by increasing the lattice spacing along the transverse directions, $\Delta x = \Delta y = 0.8$ μm, while keeping unchanged the spacing along the z axis. We further speed up the calculation by adapting dynamically the grid shape to match the density profile, reaching sizes up to $(N_x, N_y, N_z) = (520, 520, 7{,}800)$ without producing memory errors. Each simulation of the expansion dynamics takes between 16 and 24 h of wall clock time, depending on the specific value of the exposure time τ^{on}. The use of a coarser grid introduces some approximation; in particular, the peak aspect ratio for large exposure time τ^{on} is underestimated, resulting in an apparent discrepancy with the experimental data.

In order to extract the characteristic time $\tau^{\mathrm{on}}_{1/2}$ from the simulated expansion dynamics, we calculate the time τ^{on} after which the peak aspect ratio during expansion has dropped to half its initial value. To this end, the values of the aspect ratio for varying τ^{on} are interpolated, and we only consider values of the aspect ratio below 10, since larger values are experimentally not accessible, due to imaging aberrations.

Finite temperature effects. The GP equation assumes that the gas is at zero temperature. To understand how temperature affects the density response of the gas, we focus on the equilibrium case, where the speckle is loaded adiabatically. Assuming that the condensate healing length is small compared to the speckle grain size in the x and y directions, we can treat the disorder as a slowly varying potential and use a finite temperature generalization of the LDA, based on the Hartree–Fock approach. Within this theory, the condensate and the thermal densities, indicated, respectively, by n_c and n_T, satisfy the coupled equations (33)

$$n_c(\mathbf{r}) = \frac{1}{g}(\mu - V_{\mathrm{ext}}(\mathbf{r}) - 2gn_T(\mathbf{r})), \qquad [11]$$

$$n_T(\mathbf{r}) = \int\frac{\mathrm{d}^3p}{(2\pi\hbar)^3}\frac{1}{e^{\beta(\frac{p^2}{2m} - \mu + V_{\mathrm{ext}}(\mathbf{r}) + 2g(n_c(\mathbf{r}) + n_T(\mathbf{r}))} - 1},$$

where $V_{\mathrm{ext}} = V_{\mathrm{tr}} + V$ is the total external potential acting on the atoms, and $\beta = 1/(k_BT)$, with k_B being the Boltzmann constant. The chemical potential μ in the above equations must be fixed from the normalization condition $N = \int\mathrm{d}^3rn_{3D}(\mathbf{r})$, where $n_{3D}(\mathbf{r}) = n_c(\mathbf{r}) + n_T(\mathbf{r})$ is the total density. From the latter, we extract the column density and the density response, following the same procedure used for the GP numerics.

Description of Time Scales. We extract the half-life periods of the density (coherence) response by fitting the time series with Gompertz (exponential) functions (49), which we have found to adequately describe all data.

PHYSICS

Density response. After the quench into disorder, the random potential causes a spatially varying accumulation of phase $\Delta\phi = Vt/\hbar$, resulting in a velocity field according to $\mathbf{v} = \hbar/m\nabla\phi$. We can only detect density variations once their size exceeds the resolution $\alpha = 2.2\,\mu$m of our imaging system. Therefore, we are interested in the typical time $t^{\mathrm{d}}_{\mathrm{on}}$ after which the flow has traversed the distance α. Thus, we estimate $\langle|\mathbf{v}|\rangle$ in order to be able to calculate $\Delta s = 1/2\,\langle|a|\rangle\,t^2$, where $\langle|a|\rangle = \mathrm{d}\langle|\mathbf{v}|\rangle/\mathrm{d}t = \langle|\nabla V|\rangle/m$. Since the only relevant length and energy scale of the speckle in the imaging plane are given by $\langle V\rangle$ and the correlation length $\eta_{x,y}$, the magnitude of the mean speckle gradient must be proportional to $\langle V\rangle/\eta_{x,y}$. Indeed, a numerical simulation provides $\langle(\nabla V)_x\rangle = \langle(\nabla V)_y\rangle = \langle V\rangle/\eta_{x,y}$, yielding $\langle|\nabla V|\rangle = \sqrt{2}\langle V\rangle/\eta_{x,y}$. This leads to the estimation $t^{\mathrm{d}}_{\mathrm{on}} = \sqrt{2m\alpha/\langle|\nabla V|\rangle} = \sqrt{\sqrt{2}m\alpha\eta_{x,y}/\langle V\rangle}$.

Once the speckle potential is rapidly extinguished, the density redistributes to adapt to the altered external potential. We assume that the typical speed of flow is given by v. We can only detect the redistribution as long as it occurs on a length scale larger than α. This yields the estimation $t^{\mathrm{d}}_{\mathrm{off}} = \alpha/v$. Plugging in either the speed of sound v_{s}, the average thermal velocity from the Maxwell–Boltzmann distribution $\propto\sqrt{k_{\mathrm{B}}T/m}$ ($T < 100$ nK), or the maximum velocity during a classical harmonic oscillation $R_x\omega_x$ in the dipole trapping potential yields values close to the observed times. R_x denotes the Thomas–Fermi radius of the condensate along x.

Coherent hydrodynamic response. Since we attribute the breakdown of hydrodynamics to the loss of phase coherence, it must be related to the spatially varying phase accumulation after the quench. The mean phase difference between two points in the BEC after time t is $\langle\delta\phi\rangle = \langle\Delta V\rangle\,t/\hbar$, with the mean speckle potential difference $\langle\Delta V\rangle = \langle|V(\mathbf{r}) - V(\mathbf{r}')|\rangle$. From the numerical simulation, we obtain $\langle\Delta V\rangle = \langle V\rangle$, yielding $t^{\mathrm{h}}_{\mathrm{on}} = \hbar/\langle V\rangle$. In order to incorporate the differences in initial (A_{i}) and final (A_{f}) peak aspect ratio in $t^{\mathrm{h}}_{\mathrm{on}}$, we write $t^{\mathrm{h}}_{\mathrm{on}} = \hbar/\langle V\rangle \times \Delta A/A_{\mathrm{i}}$, where $\Delta A = A_{\mathrm{i}} - A_{\mathrm{f}}$.

As the time scale of reoccurrence of hydrodynamics, we find $t^{\mathrm{h}}_{\mathrm{off}} = 2R_y/v_{\mathrm{s}} = 2\sqrt{2}/\omega_y$, where $R_y = \sqrt{2\mu/m}/\omega_y$ is the Thomas–Fermi radius along y. Similar as for $t^{\mathrm{h}}_{\mathrm{on}}$, we write $t^{\mathrm{h}}_{\mathrm{off}} = 2\sqrt{2}/\omega_y \times |\Delta A|\,/A_{\mathrm{f}}$.

Calculation of the Phase Correlation Length. We get the correlation length of the phase σ_ϕ by calculating the autocorrelation function

$$\mathrm{AC}_\phi\,(\delta x, \delta y) = \int f(x,y) f^*(x+\delta x, y+\delta y)\mathrm{d}x\mathrm{d}y \qquad [12]$$

of the function $f(x,y) = \sqrt{n(x,y)} \times \exp\,(i\phi(x,y,z=0))$, which is the product of the phase factor in the central plane of the cloud and the square root of the integrated column density, the latter of which accounts for the inhomogeneous density distribution. Both the phase factor and column density are obtained from the numerical simulation of the GP equation. To reduce the computational effort, we limit the evaluation to the central x–y plane at $z = 0$. Hence, exploiting the Wiener–Khinchin theorem (54), the autocorrelation function is given by

$$\mathrm{AC}_\phi\,(\delta x, \delta y) = \mathcal{F}^{-1}\,(\mathrm{PSD})\,(\delta x, \delta y)\,, \qquad [13]$$

where

$$\mathrm{PSD} = \left|\mathcal{F}\left(\exp\,(i\phi(x,y,z=0))\,\sqrt{n(x,y)}\right)(k_x,k_y)\right|^2 \qquad [14]$$

is the power spectral density with the spatial frequencies (k_x, k_y). We evaluate the Fourier transform $\mathcal{F}$ numerically using a fast Fourier transform algorithm. The phase correlation length σ_ϕ in x (y) direction is defined as the distance along δx (δy) across which AC_ϕ drops to $1 - 1/e \approx 63$ % of its value at $\delta x = \delta y = 0$.

Data Availability. All study data are included in the article and/or *SI Appendix*.

ACKNOWLEDGMENTS. We thank B. Gänger and J. Phieler for help in the construction of the apparatus, and J. Anglin for valuable discussions. We also acknowledge comments by M. Modugno and S. Pilati on the manuscript, which helped us improve the presentation. This work was supported by the Deutsche Forschungsgemeinschaft (DFG, German Research Foundation) via the Collaborative Research Center Sonderforschungsbereich SFB/TR185 (Project 277625399). B.N. received support from a DFG Fellowship through the Excellence Initiative by the Graduate School Materials Science in Mainz (program GSC 266). J.K. was supported by the Max Planck Graduate Center with the Johannes Gutenberg-Universität Mainz. This work was granted access to the computational resources of the National Computing Center for Higher Education (CINES) under allocations 2019-A0060507629 and 2020-A0080507629 supplied by Grand Equipement National de Calcul Intensif (GENCI).

1. C. L. Degen, F. Reinhard, P. Cappellaro, Quantum sensing. *Rev. Mod. Phys.* **89**, 035002 (2017).
2. J. T. Devreese, J. Tempere, Superfluidity from He-4 to ultracold atomic condensed systems. *Physica C Supercond.* **479**, 36–40 (2012).
3. K. Gavroglu, Y. Goudaroulis, Understanding macroscopic quantum phenomena: The history of superfluidity 1941–1955. *Ann. Sci.* **45**, 367–385 (1988).
4. W. Ketterle, M. W. Zwierlein, "Making, probing and understanding ultracold Fermi gases" in *Proceedings of the International School of Physics "Enrico Fermi,"* C. S. M. Inguscio, W. Ketterle, Eds. (IOS Press, 2007), **vol. 164**, pp. 247–422.
5. M. R. Andrews *et al.*, Observation of interference between two Bose condensates. *Science* **275**, 637–641 (1997).
6. E. W. Hagley *et al.*, Measurement of the coherence of a Bose-Einstein condensate. *Phys. Rev. Lett.* **83**, 3112–3115 (1999).
7. I. Bloch, T. W. Hansch, T. Esslinger, Measurement of the spatial coherence of a trapped Bose gas at the phase transition. *Nature* **403**, 166–170 (2000).
8. J. K. Chin *et al.*, Evidence for superfluidity of ultracold fermions in an optical lattice. *Nature* **443**, 961–964 (2006).
9. Z. Hadzibabic, P. Krüger, M. Cheneau, B. Battelier, J. Dalibard, Berezinskii-Kosterlitz-Thouless crossover in a trapped atomic gas. *Nature* **441**, 1118–1121 (2006).
10. S. Ritter *et al.*, Observing the formation of long-range order during Bose-Einstein condensation. *Phys. Rev. Lett.* **98**, 090402 (2007).
11. S. Hofferberth, I. Lesanovsky, B. Fischer, T. Schumm, J. Schmiedmayer, Non-equilibrium coherence dynamics in one-dimensional Bose gases. *Nature* **449**, 324–327 (2007).
12. Y. P. Chen *et al.*, Phase coherence and superfluid-insulator transition in a disordered Bose-Einstein condensate. *Phys. Rev. A* **77**, 033632 (2008).
13. K. W. Madison, F. Chevy, W. Wohlleben, J. Dalibard, Vortex formation in a stirred Bose-Einstein condensate. *Phys. Rev. Lett.* **84**, 806–809 (2000).
14. M. W. Zwierlein, J. R. Abo-Shaeer, A. Schirotzek, C. H. Schunck, W. Ketterle, Vortices and superfluidity in a strongly interacting Fermi gas. *Nature* **435**, 1047–1051 (2005).
15. B. V. Svistunov, Superfluid turbulence in the low-temperature limit. *Phys. Rev. B Condens. Matter* **52**, 3647–3653 (1995).
16. T. Zhang, S. W. Van Sciver, Large-scale turbulent flow around a cylinder in counterflow superfluid ^{4}He (HeII). *Nat. Phys.* **1**, 36–38 (2005).
17. G. P. Bewley, M. S. Paoletti, K. R. Sreenivasan, D. P. Lathrop, Characterization of reconnecting vortices in superfluid helium. *Proc. Natl. Acad. Sci. U.S.A.* **105**, 13707–13710 (2008).
18. L. F. Gomez *et al.*, Helium superfluidity. Shapes and vorticities of superfluid helium nanodroplets. *Science* **345**, 906–909 (2014).
19. K. Thompson *et al.*, Evidence of power law behavior in the momentum distribution of a turbulent trapped Bose–Einstein condensate. *Laser Phys. Lett.* **11**, 015501 (2014).
20. A. C. White, B. P. Anderson, V. S. Bagnato, Vortices and turbulence in trapped atomic condensates. *Proc. Natl. Acad. Sci. U.S.A.* **111**, 4719–4726 (2014).
21. N. Navon, A. L. Gaunt, R. P. Smith, Z. Hadzibabic, Emergence of a turbulent cascade in a quantum gas. *Nature* **539**, 72–75 (2016).
22. M. Greiner, O. Mandel, T. W. Hänsch, I. Bloch, Collapse and revival of the matter wave field of a Bose-Einstein condensate. *Nature* **419**, 51–54 (2002).
23. U. Schneider *et al.*, Fermionic transport and out-of-equilibrium dynamics in a homogeneous Hubbard model with ultracold atoms. *Nat. Phys.* **8**, 213–218 (2012).
24. F. Meinert *et al.*, Quantum quench in an atomic one-dimensional Ising chain. *Phys. Rev. Lett.* **111**, 053003 (2013).
25. M. Cetina *et al.*, Ultrafast many-body interferometry of impurities coupled to a Fermi sea. *Science* **354**, 96–99 (2016).
26. C. Meldgin *et al.*, Probing the Bose glass–superfluid transition using quantum quenches of disorder. *Nat. Phys.* **12**, 646–649 (2016).
27. R. Grimm, "Ultracold Fermi gases in the BEC-BCS crossover: A review from the Innsbruck perspective" in *Proceedings of the International School of Physics "Enrico Fermi,"* C. S. M. Inguscio, W. Ketterle, Eds. (IOS Press, 2007), **vol. 164**, pp. 413–462.
28. R. C. Kuhn, O. Sigwarth, C. Miniatura, D. Delande, C. A. Müller, Coherent matter wave transport in speckle potentials. *New J. Phys.* **9**, 161 (2007).
29. J. E. Lye *et al.*, Bose-Einstein condensate in a random potential. *Phys. Rev. Lett.* **95**, 070401 (2005).
30. M. Modugno, Collective dynamics and expansion of a Bose-Einstein condensate in a random potential. *Phys. Rev. A* **73**, 013606 (2006).
31. C. J. Pethick, H. Smith, *Bose–Einstein Condensation in Dilute Gases* (Cambridge University Press, ed. 1, 2002).
32. L. Sanchez-Palencia, Smoothing effect and delocalization of interacting Bose-Einstein condensates in random potentials. *Phys. Rev. A* **74**, 053625 (2006).
33. S. Pilati, S. Giorgini, M. Modugno, N. Prokof'ev, Dilute Bose gas with correlated disorder: A path integral Monte Carlo study. *New J. Phys.* **12**, 073003 (2010).
34. S. Giorgini, J. Boronat, J. Casulleras, Ground state of a homogeneous Bose gas: A diffusion Monte Carlo calculation. *Phys. Rev. A* **60**, 5129–5132 (1999).
35. R. J. Fletcher *et al.*, Elliptic flow in a strongly interacting normal Bose gas. *Phys. Rev. A (Coll. Park)* **98**, 011601 (2018).
36. I. Shvarchuck *et al.*, Hydrodynamic behavior in expanding thermal clouds of ^{87}Rb. *Phys. Rev. A* **68**, 063603 (2003).
37. I. Shvarchuck *et al.*, Bose-Einstein condensation into nonequilibrium States studied by condensate focusing. *Phys. Rev. Lett.* **89**, 270404 (2002).
38. P. Pedri, D. Guéry-Odelin, S. Stringari, Dynamics of a classical gas including dissipative and mean-field effects. *Phys. Rev. A* **68**, 043608 (2003).

39. E. P. Gross, Structure of a quantized vortex in boson systems. *Nuovo Cim.* **20**, 454–477 (1961).
40. L. P. Pitaevskii, Vortex lines in an imperfect Bose gas. *J. Exp. Theor. Phys.* **40**, 646–651 (1961).
41. Y. Kagan, E. L. Surkov, G. V. Shlyapnikov, Evolution of a Bose gas in anisotropic time-dependent traps. *Phys. Rev. A* **55**, R18–R21 (1997).
42. P. O. Fedichev, G. V. Shlyapnikov, J. T. M. Walraven, Damping of low-energy excitations of a trapped Bose-Einstein condensate at finite temperatures. *Phys. Rev. Lett.* **80**, 2269–2272 (1998).
43. E. A. L. Henn, J. A. Seman, G. Roati, K. M. F. Magalhães, V. S. Bagnato, Emergence of turbulence in an oscillating Bose-Einstein condensate. *Phys. Rev. Lett.* **103**, 045301 (2009).
44. M. Kobayashi, M. Tsubota, Kolmogorov spectrum of superfluid turbulence: Numerical analysis of the Gross-Pitaevskii equation with a small-scale dissipation. *Phys. Rev. Lett.* **94**, 065302 (2005).
45. B. Gänger, J. Phieler, B. Nagler, A. Widera, A versatile apparatus for fermionic lithium quantum gases based on an interference-filter laser system. *Rev. Sci. Instrum.* **89**, 093105 (2018).
46. G. Zürn *et al.*, Precise characterization of ^{6}Li Feshbach resonances using trap-sideband-resolved RF spectroscopy of weakly bound molecules. *Phys. Rev. Lett.* **110**, 135301 (2013).
47. G. Reinaudi, T. Lahaye, Z. Wang, D. Guéry-Odelin, Strong saturation absorption imaging of dense clouds of ultracold atoms. *Opt. Lett.* **32**, 3143–3145 (2007).
48. M. Naraschewski, D. M. Stamper-Kurn, Analytical description of a trapped semi-ideal Bose gas at finite temperature. *Phys. Rev. A* **58**, 2423–2426 (1998).
49. E. W. Weisstein, *Gompertz curve*. *MathWorld* (2019). https://mathworld.wolfram.com/Gompertz-curve.html. Accessed 31 October 2019.
50. J. E. Goodman, *Speckle Phenomena in Optics: Theory and Applications* (Roberts & Company, 2007).
51. V. V. Volchkov *et al.*, Measurement of spectral functions of ultracold atoms in disordered potentials. *Phys. Rev. Lett.* **120**, 060404 (2018).
52. L. Young *et al.*, OpenMP GNU and Intel Fortran programs for solving the time-dependent Gross–Pitaevskii equation. *Comput. Phys. Commun.* **220**, 503–506 (2017).
53. P. Muruganandam, S. Adhikari, Fortran programs for the time-dependent Gross–Pitaevskii equation in a fully anisotropic trap. *Comput. Phys. Commun.* **180**, 1888–1912 (2009).
54. N. Wiener, Generalized harmonic analysis. *Acta Math.* **55**, 117–258 (1930).